Letter

Interfacial electron-phonon coupling and quantum confinement in ultrathin Yb films on graphite

Yi Wu,[1,2,*] Wenhao Zhang,[1,*] Yuan Fang,[1,2] Shuai Lu,[3] Li Wang,[3] Peng Li,[1,2] Zhongzheng Wu,[1,2] Zhiguang Xiao,[1,2] Chao Cao,[4] Xiaoxiong Wang,[5] Fang-Sen Li,[6] Yi Yin,[1,7,†] Tai-Chang Chiang,[8] and Yang Liu[1,2,7,‡]

[1]*Zhejiang Province Key Laboratory of Quantum Technology and Device, Department of Physics, Zhejiang University, Hangzhou 310058, China*

[2]*Center for Correlated Matter, Zhejiang University, Hangzhou 310058, China*

[3]*Suzhou Institute of Nano-Tech and Nano-Bionics (SINANO), CAS, Suzhou 215123, China*

[4]*Department of Physics, Hangzhou Normal University, Hangzhou 311121, China*

[5]*College of Science, Nanjing University of Science and Technology, Nanjing 210094, China*

[6]*Vacuum Interconnected Nanotech Workstation (Nano-X), Suzhou Institute of Nano-Tech and Nano-Bionics (SINANO), CAS, Suzhou 215123, China*

[7]*Collaborative Innovation Center of Advanced Microstructures, Nanjing University, Nanjing 210093, China*

[8]*Department of Physics and Frederick Seitz Materials Research Laboratory, University of Illinois at Urbana-Champaign, Urbana, Illinois 61801, USA*

(Received 21 May 2021; revised 4 September 2021; accepted 27 September 2021; published 7 October 2021)

Interfacial electron-phonon coupling in ultrathin films has attracted much interest recently. Here, by combining angle-resolved photoemission spectroscopy and scanning tunneling microscopy, we report quantized electronic states and strong interfacial electron-phonon coupling in ultrathin Yb films on graphite. We observed clear kinks in the energy-momentum dispersion of quantum well states, and the kink positions agree well with the energies of optical phonons of graphite. The extracted coupling strength λ is largest for the thinnest film with a preferred ("magic") thickness of four monolayers and exhibits a strong band dependence, which can be qualitatively accounted for by a simple model. The interfacial electron-phonon coupling also gives rise to characteristic steplike structures in the dI/dV spectra, implying dominant coupling with the phonons with zero in-plane momentum. A Lifshitz transition occurs at higher coverage, where quantum well states derived mainly from $5d$ electrons dominate near the Fermi level and possess large effective mass (up to $\sim 19\ m_e$). Our results highlight the potentially important role of interfacial electron-phonon interaction for ultrathin films and provide spectroscopic insight to understand this cross-interface fermion-boson interaction.

DOI: 10.1103/PhysRevB.104.L161402

Electron-phonon coupling (EPC) plays an important role in condensed matter physics; it can drive superconductivity (SC) and charge-density-wave formation [1]. While EPC in bulk materials has been studied extensively, much less is understood about interfacial EPC in ultrathin films grown on substrates. Because of the abrupt change in the crystal potential at the interface [2], EPC at the interface can be much stronger than that in the bulk, possibly leading to novel consequences. A notable example is the single-layer FeSe grown on $SrTiO_3(001)$, for which a SC transition temperature T_C up to 60 K has been reported [3–8], almost an order of magnitude higher than the bulk T_C (8 K). This remarkable enhancement has been partially attributed to a large interfacial EPC [9–12]. Experimental signatures of interfacial EPC in thin films have been identified by angle-resolved photoemission spectroscopy (ARPES) via shake-off bands due to bosonic excitations [9] or temperature-dependent broadening of quasiparticle bands [2]. Theoretically, when the substrate phonon energy is much smaller than the conduction band width of the film, interfacial EPC could also give rise to kinks in the quasiparticle dispersions [13], similar to those observed in bulk samples such as cuprates [14–16] or in simple metal surfaces [17,18]. Here, we report evidence of such kinks for the quantum well states (QWSs) in ultrathin Yb films grown on graphite, implying a band-dependent coupling constant λ as large as 0.6. The interfacial EPC is further supported by measurements from scanning tunneling microscopy (STM), which reveal steplike features in the dI/dV curves caused by the phonon-mediated inelastic tunneling. These spectroscopic signatures of interfacial EPC can be important for characterizing and understanding this cross-interface interaction.

Our work on Yb films is also motivated by earlier studies suggesting that $4f$ electrons might play an important role in the Fermi surface (FS) of ultrathin Yb films at low temperatures [19], analogous to its electron counterpart Ce with one $4f$ electron [20–22]. Some recent work further showed that bulk Yb under pressure could undergo valence fluctuations associated with the $4f$ occupancy and exhibit a SC transition at temperatures up to 6 K [23]. Therefore it is important to elucidate the underlying electronic structure and understand the role of $4f$ electrons and electronic correlation. Prior stud-

*These authors contributed equally to this work.
†yiyin@zju.edu.cn
‡yangliuphys@zju.edu.cn

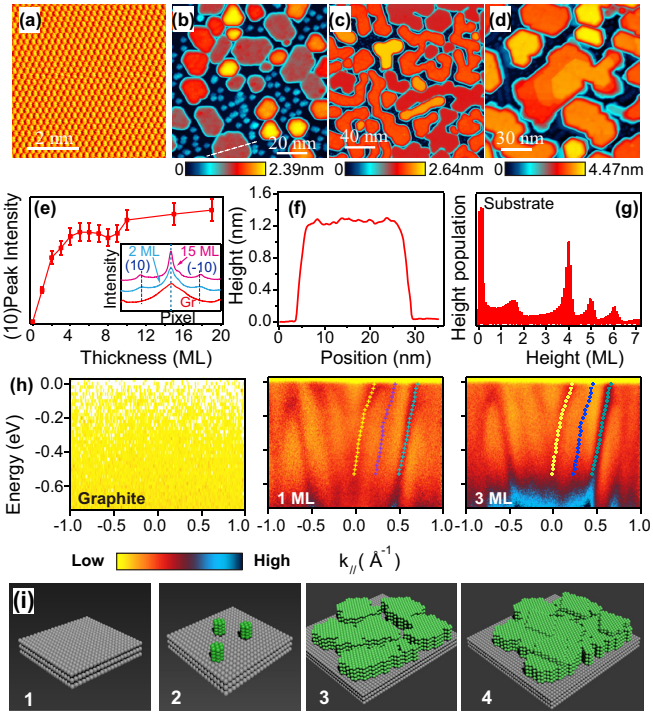

FIG. 1. Film growth and formation of magic-height islands. (a)–(d) STM images of clean graphite substrate (a) and Yb films with increasing nominal coverages: 2.5 MLs (b), 6 MLs (c), and 9.5 MLs (d). (e) The (1,0) peak intensity from RHEED as a function of film coverage, showing a slope change near three MLs. The inset is a line cut of RHEED intensity, implying possibly a small lattice change between 2 MLs and 15 MLs. (f) Height profile of a four-ML magic island along the dashed line shown in Fig. 1(b). (g) The island height distribution for a film with 2.5-ML coverage. (h) ARPES spectra for the substrate and for Yb films with one- and three-ML nominal coverages. (i) Cartoons illustrating different stages of film growth (stages 1–4).

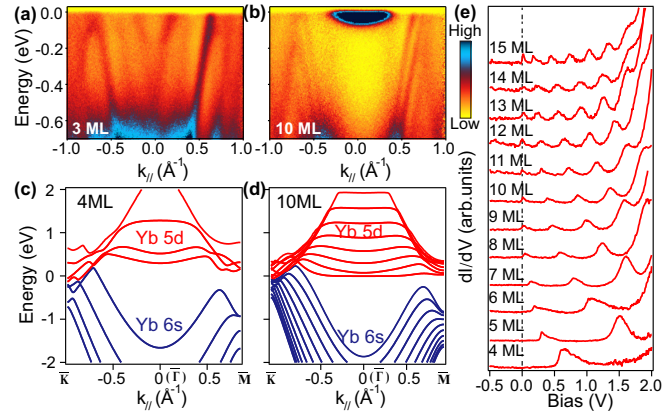

FIG. 2. Thickness-driven Lifshitz transition in Yb films. (a) and (b) ARPES spectra of a three-ML film (the magic-height islands) (a) and a ten-ML film (thick film) (b). In (a) the three-ML data are displayed, as the four-ML data contain a slight admixture from higher-thickness films due to inevitable roughness [27]. (c) and (d) The calculated band structures for four-ML (c) and ten-ML (d) film along two high-symmetry directions, obtained from slab calculations. (e) The dI/dV curves of Yb films with different thicknesses, from STM measurements.

ies of Yb films on W(110) [24–26], while informative, did not provide the fine electronic structures near the Fermi level (E_F) to address the issues of $4f$-$5d$ occupancy and interfacial EPC effects.

Yb films were grown on graphite at room temperature using molecular beam epitaxy (MBE). ARPES and STM measurements were performed at low temperatures (~20 K for ARPES and ~4.7 K for STM) by transferring the sample under ultrahigh vacuum from the MBE chamber to the ARPES or STM chamber. More growth and measurement details can be found in the Supplemental Material [27]. Figures 1(a)–1(d) show the STM images of the Yb films at various nominal coverages (the coverage refers to the amount of Yb deposited onto graphite [27]). At low coverage, flat islands with a preferred height of four monolayers (MLs) can be readily identified [Figs. 1(b) and 1(f)]. The height distribution in Fig. 1(g) reveals the preferred formation of a four-ML island, which is also supported by measurements from reflection high-energy electron diffraction (RHEED) in Fig. 1(e), showing a slope change in the diffraction intensity near a nominal coverage of four MLs. Figure 1(i) schematically illustrates the growth behavior: At low coverage (stages 1–3), "magic" islands with four-ML height are formed preferably, and the islands grow laterally to cover the surface below ~4 MLs; above four MLs (stage 4), islands with higher thickness form with appreciable roughness. Such magic islands with preferred height have been reported previously for metallic thin-film systems [28–30], most notably in Pb/Si(111) [31,32]. The formation of a magic-height island is generally driven by the total energy minimization, where both the electronic quantization and interfacial effects could play an important role.

ARPES spectra for Yb films are shown in Figs. 1(h), 2(a), and 2(b) (more systematic data are included in Fig. S2 of the Supplemental Material [27]). The graphite substrate shows no discernible features within the displayed energy and momentum ranges. Approximately parabolic bands emerge as Yb is deposited; these correspond to quantum well states (QWSs) of Yb films [33]. The energies and perpendicular momenta of these QWSs are governed by the Bohr-Sommerfeld quantization condition [33]:

$$2k_z(E)Nt + \varphi_s + \varphi_i = 2n\pi\,, \tag{1}$$

where $k_z(E)$ is the perpendicular momentum as a function of energy E, N is the film thickness in MLs, t is the thickness of one ML, $\varphi_s(\varphi_i)$ is the phase shift at the surface (interface), and n is the quantum number of each QWS subband. As N increases, the QWS energies should change (most obviously for thinner films) and more subbands should emerge within the same energy range [34,35]. However, the results for films of less than four MLs show approximately the same set of subbands (Fig. 1(h) and also Fig. S2 of the Supplemental Material [27]), and only the emission intensity increases with coverage. This confirms the formation of four-ML magic islands with identically quantized electronic states. For coverages above four MLs, the QWSs become more closely spaced due to larger thickness (Fig. 2(b) and also Fig. S2 of the Supplemental Material [27]). Note that the energy positions of

QWSs are quite different for the three-ML (magic thickness) film and ten-ML (thick) film: The parabolic bands below −0.4 eV near $\bar{\Gamma}$ are shifted to lower energies for thicker films, and simultaneously, heavy electron bands emerge right near E_F [Figs. 2(a) and 2(b)], signaling a thickness-driven Lifshitz transition. We mention that the graphite substrate used here is highly oriented pyrolytic graphite. Hence the ARPES spectra from the Yb films contain averaged contributions from domains with different in-plane orientations. Since we are mainly concerned about isotropic QWSs derived from 6*s* electrons, the in-plane orientational averaging does not affect our main results, as evidenced by the well-defined QWSs extending to large in-plane momentum.

Figures 2(c) and 2(d) show the calculated band structures for the four-ML and ten-ML films, obtained from slab calculations using density functional theory (DFT). The calculations can reasonably reproduce the experimental data in Figs. 2(a) and 2(b), particularly the thickness-driven Lifshitz transition, although slight quantitative differences are present. The parabolic bands near $\bar{\Gamma}$ below −1 eV are derived from the Yb 6*s* states, and they shift to lower energies for the ten-ML film, qualitatively consistent with the experimental results. Detailed comparison with DFT calculations suggests that the tensile strain for the magic-thickness film, ∼5% inferred from the RHEED measurements shown in Fig. 1(e), could be important for this energy shift (Figs. S1 and S4 of the Supplemental Material [27]), in addition to the thickness-dependent electronic quantization. Another major difference between the four-ML and ten-ML films is the emergence in the latter of an intense flat band right below E_F. This band moves down with increasing thickness, and its estimated effective mass can be up to $\sim 19\, m_e$ (see Fig. S6 of the Supplemental Material [27]). It is tempting to associate this heavy band with the Yb 4*f* electrons, especially in view of earlier reports of a temperature-dependent phase transition in ultrathin Yb films [19], implying a possible analogy to the α-γ transition in Ce [20]. However, DFT calculations suggest that this heavy electron band is mostly derived from the Yb 5*d* states. This is also supported by the measured energy positions of shallow $4f_{5/2}$ and $4f_{7/2}$ states, which correspond to an electronic configuration of $4f^{14}$ (Fig. S2 of the Supplemental Material [27]). Thus valence fluctuations or instabilities involving the $4f^{13}$ configuration as suggested in earlier studies are irrelevant in the present case, and the Yb 4*f* electrons play a minor role near E_F. The thickness-driven Lifshitz transition can be better illustrated from the thickness-dependent dI/dV curves from STM shown in Fig. 2(e). Here, the occupied states below E_F (probed by ARPES) are rather weak, but the unoccupied QWSs (mainly from Yb 5*d*) above E_F can be clearly observed. The Yb 5*d* QWS with the lowest energy is well above E_F for the magic-thickness film, and it approaches E_F with increasing thickness, eventually crossing E_F at ∼8 MLs. Such a large shift with thickness is likely caused by quantum confinement and the strain effect [27,36]. We note that the QWS positions in Fig. 2(e) differ slightly from those in Figs. 2(c) and 2(d), likely due to electron correlation effects.

Strong kinks in the QWS dispersions can be observed for the magic-thickness film [Fig. 3(a)], suggesting a large interfacial EPC. In Fig. 3(a), the QWS subbands are labeled in terms of $n = 0, 1, 2, \ldots$, with $k_z(E)$ in Eq. (1) defined

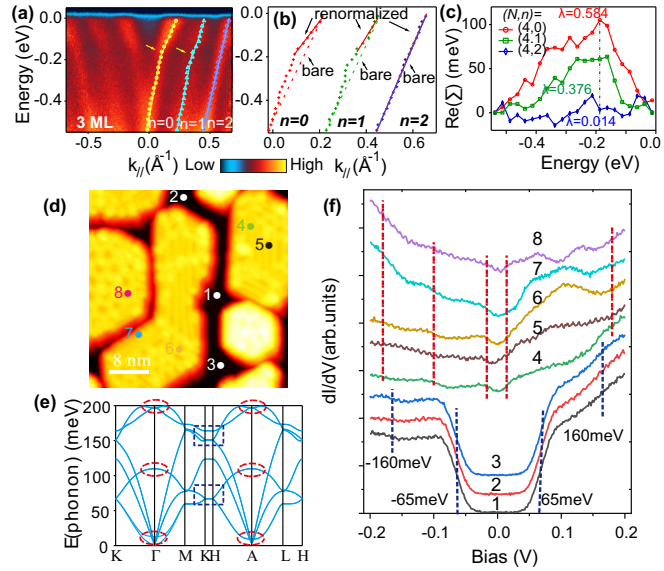

FIG. 3. Band dispersion kinks and phonon-mediated tunneling in magic-thickness Yb films from interfacial EPC. (a) ARPES spectra near E_F for the magic-thickness film. The extracted band dispersions (colored symbols) are overlaid on top of the experimental data. (b) Extracted band dispersions (colored pluses) and the extrapolated bare-band dispersion without EPC (dash-dotted curves). (c) Extracted real part of the self-energy and λ for each QWS labeled by (N, n). (d) A typical STM image of magic-thickness islands. (e) Calculated phonon dispersion relations for graphite. Dashed ovals and rectangular boxes indicate phonons contributing to inelastic tunneling for magic-thickness Yb films and the graphite substrate, respectively. (f) dI/dV curves at different positions labeled in Fig. 3(d): Positions 1–3 are on bare graphite; positions 4–8 are on Yb islands. Vertical dashed lines indicate the steplike features due to the phonon-mediated inelastic tunneling.

with respect to the zone boundary [33]. The kink is particularly strong for the $n = 0$ subband and becomes obviously weaker for larger n. Following the standard procedure of analyzing EPC in bulk samples [16], we extract the bare-band dispersions ε_k (without EPC) by extrapolating the QWS dispersion from far below E_F, shown as dash-dotted curves in Fig. 3(b). The real part of the self-energy, Re $\Sigma(E)$, is the difference between the experimental band $E(k)$ [colored pluses in Fig. 3(b)] and the bare-band ε_k. The resulting Re $\Sigma(E)$'s from such analysis [Fig. 3(c)] show broad peaks at approximately −0.18 eV, particularly for $n = 0$ and $n = 1$. This energy does not correspond to any known bosonic excitations from Yb itself [37]; instead, it corresponds well to the in-plane optical phonons of graphite, whose energies range from 150 to 200 meV [Fig. 3(e)] [38,39]. This implies that the kinks likely originate from the interfacial EPC. Prior studies from FeSe on $SrTiO_3(001)$ suggest that interfacial EPC could be strongly peaked at $q_{||} = 0$ due to a large ratio between the in-plane and out-of-plane dielectric constants in two-dimensional films [9,40,41]. Therefore the kink at approximately −0.18 eV could be attributed to the dominant coupling with the in-plane optical phonons near the Γ/A point(s). The strength of the interfacial EPC λ can be

estimated from

$$\lambda = \frac{\left(\frac{d\varepsilon}{dk}\right)_{\text{bare}}}{\left(\frac{dE}{dk}\right)_{\text{renormalized}}} - 1, \tag{2}$$

which yields $\lambda \sim 0.58$, 0.38, and 0.01 for $n = 0$, 1, and 2, respectively.

Evidence of interfacial EPC can also be found in STM via the phonon-enhanced conductance in the dI/dV spectra. Specifically, the dI/dV spectra could exhibit steplike features at the corresponding phonon energies due to sudden onset of phonon-mediated inelastic tunneling [42–44]. Such phonon-induced steplike structures have been well documented for graphene and graphite [42,43,45] and are reproduced here for the graphite substrate [Figs. 3(d) and 3(f)]. Due to the special band structure of graphene and graphite involving only the Dirac bands from the K or H point near E_F, the phonon-mediated inelastic tunneling is dominated by the phonons near the K or H point(s), i.e., the out-of-plane (in-plane) phonons at ~65 (~160) meV shown in Fig. 3(e), leading to phonon-induced steps marked by the vertical blue dashed lines in Fig. 3(f). For the magic-thickness Yb films grown on graphite, the typical dI/dV spectra show steplike features at roughly ± 180, -100, and ± 15 meV, which seem to agree very well with the phonon energies of graphite at the Γ or A point. The results are also consistent with recent studies suggesting that the interfacial EPC could be dominated by coupling with the $q_{||} = 0$ phonons [9,40]. We mention that there are some site-dependent variations near the 100-meV region in the dI/dV curves, which is likely due to different surface structures or electronic reconstructions. In comparison, the phonon kinks in ARPES spectra are dominated by the high-lying phonons at ~180 meV, while the kinks from other phonon modes appear to be much weaker. The difference between ARPES and STM might be related to the different photoexcitation and tunneling matrix elements, which have also been observed in bare graphene [42,46]. After all, these two experimental methods involve very different physical processes, i.e., the momentum-integrated electron tunneling for STM vs the photoexcitation dipole transition for ARPES.

Due to the interfacial nature, the strength of interfacial EPC is expected to decay rapidly with film thickness. Indeed, the kink feature in ARPES spectra diminishes quickly with increasing film thickness (Figs. 4(a) and 4(b) and also Fig. S5 of the Supplemental Material [27]). The extracted dispersion for the $n = 0$ QWS of ten-ML film shows possibly a very weak kink at approximately -0.2 eV, and no evidence of a band kink can be identified for the 20-ML film.

The large subband (n) and thickness (N) dependence of λ observed here is likely a common characteristic for interfacial EPC, distinct from EPC in bulk. Such n and N dependence could be qualitatively accounted for by a simple model proposed in Ref. [2]: Assuming that the interfacial EPC arises from the large potential gradient at the interface and can be described within the rigid-ion approximation, the strength of interfacial EPC (λ) is proportional to the fourth power of the amplitude of the QWS wave function (or square of the probability density) at the interface. For the $n = 0$ QWS, the probability density along the z direction has a maximum at each Yb atomic layer [see Fig. 4(c) for a simple illustration]. As N increases, the normalized probability density at each atomic layer diminishes correspondingly. This dilution effect leads to a reduction in the probably density at the interface, and λ should decay approximately as $1/N^2$. For a given N, increasing n by 1 results in a reduction in the number of probability density maxima in the film by 1, as illustrated by the top three curves in Fig. 4(c). Hence the probability density maximum next to the interface moves inward toward the center of the film. The resulting decrease in the probability density at the interface should cause λ to decrease considerably. Thus the dependence of λ on N and n can be qualitatively explained by this simple model. A quantitative analysis, however, is difficult at the moment and requires detailed knowledge of the interfacial structure and the corresponding electronic wave functions. The formation of magic-thickness islands with large interfacial EPC implies large interfacial interaction, but the microscopic origin requires further studies in the future. It is interesting to note that most metallic thin films grown on graphite are close to being freestanding due to the weak van der Waals bonding at the interface, but the current Yb/graphite system seems to be different, likely due to the small electronegativity of Yb (hence strong tendency to form ionic bonds).

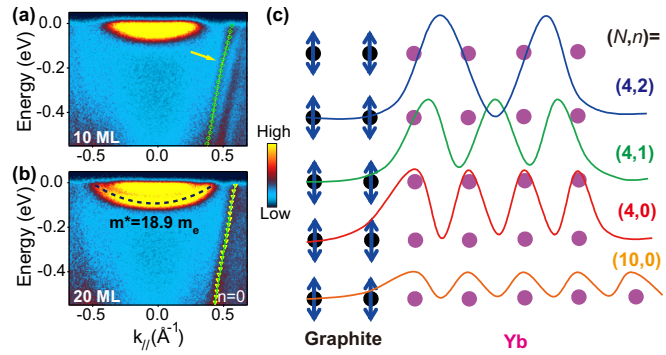

FIG. 4. The thickness (N) and subband (n) dependence of interfacial EPC coupling strength λ. (a) and (b) ARPES spectra for 10-ML (a) and 20-ML (b) film near E_F. The dispersion of the $n = 0$ QWS subband is extracted and highlighted. A yellow arrow indicates a possible kink for the ten-ML film. A parabolic fitting to the heavy electron band right below E_F is shown for the 20-ML film. (c) Simple drawings of the probability density of QWSs [labeled by (N, n)] near the Yb/graphite interface. The probability density is shown as curves, with their zero positions offset vertically for clarity.

Our results therefore demonstrate that large interfacial EPC is present in ultrathin Yb films grown on graphite, which is manifested by the kinks in the QWS dispersion measured from ARPES and the phonon-induced steplike features in the dI/dV curves obtained from STM. The interfacial EPC is strongest for the magic-thickness film with $N = 4$ MLs and for the $n = 0$ QWS, whose wave function has the largest interfacial weight. Detailed analysis of the ARPES and STM results suggests that the interfacial EPC is likely dominated by coupling with phonons with zero in-plane momentum. It is interesting that such interfacial interaction can be detected by surface-sensitive probes such as ARPES and STM, although previous studies have already shown that QWS could mediate magnetic coupling at the interface [47] and couple

coherently with the substrate electronic states [48]. A thickness-driven Lifshitz transition related to Yb $5d$ occupancy is also observed, leading to heavy quasiparticle bands near E_F with effective mass $\sim 19\ m_e$, which is likely relevant to the easily tunable properties of Yb films [19] or bulk Yb [23]. All of these observations indicate that the Yb/graphite system is unusual with interesting properties that are governed by a delicate interplay between quantum confinement, interfacial EPC, and electronic phase transition. Our extracted coupling constant λ in the Yb films can be as high as 0.6, exceeding the Bardeen-Cooper-Schrieffer threshold for SC. It would be desirable in the future to perform lower-temperature STM measurements to explore the possibility of the interfacial SC. Finally, it would be very interesting to perform similar spectroscopic studies on other $4f$-electron ultrathin films, to explore the interplay between quantum confinement and strong electron correlations from $4f$ electrons [49].

This work is supported by the National Key R&D Program of the MOST of China (Grants No. 2017YFA0303100, No. 2016YFA0300203, and No. 2019YFA0308602), the National Science Foundation of China (Grants No. 11674280 and No. 11604366), the Key R&D Program of Zhejiang Province, China (Grant No. 2021C01002), and the Fundamental Research Funds for the Central Universities. T.-C.C. acknowledges support from the U.S. Department of Energy under Grant No. DE-FG02-07ER46383. X.W. acknowledges support from the Fundamental Research Funds for the Central Universities (Grant No. 30917011338).

[1] G. Grimvall, *The Electron-Phonon Interaction in Metals*, Series of Monographs on Selected Topics in Solid State Physics Vol. 16 (North-Holland, Amsterdam, 1981).
[2] D.-A. Luh, T. Miller, J. J. Paggel, and T.-C. Chiang, Phys. Rev. Lett. **88**, 256802 (2002).
[3] Q.-Y. Wang, Z. Li, W.-H. Zhang, Z.-C. Zhang, J.-S. Zhang, W. Li, H. Ding, Y.-B. Ou, P. Deng, K. Chang, J. Wen, C.-L. Song, K. He, J.-F. Jia, S.-H. Ji, Y.-Y. Wang, L.-L. Wang, X. Chen, X.-C. Ma, and Q.-K. Xue, Chin. Phys. Lett. **29**, 037402 (2012).
[4] D. Liu, W. Zhang, D. Mou, J. He, Y. B. Ou, Q. Y. Wang, Z. Li, L. Wang, L. Zhao, S. He, Y. Peng, X. Liu, C. Chen, L. Yu, G. Liu, X. Dong, J. Zhang, C. Chen, Z. Xu, J. Hu *et al.*, Nat. Commun. **53**, 931 (2012).
[5] W.-H. Zhang, Y. Sun, J.-S. Zhang, F.-S. Li, M.-H. Guo, Y.-F. Zhao, H.-M. Zhang, J.-P. Peng, Y. Xing, H.-C. Wang, T. Fujita, A. Hirata, Z. Li, H. Ding, C.-J. Tang, M. Wang, Q.-Y. Wang, K. He, S.-H. Ji, X. Chen *et al.*, Chin. Phys. Lett. **31**, 017401 (2014).
[6] R. Peng, X. P. Shen, X. Xie, H. C. Xu, S. Y. Tan, M. Xia, T. Zhang, H. Y. Cao, X. G. Gong, J. P. Hu, B. P. Xie, and D. L. Feng, Phys. Rev. Lett. **112**, 107001 (2014).
[7] R. Peng, H. C. Xu, S. Y. Tan, H. Y. Cao, M. Xia, X. P. Shen, Z. C. Huang, C. Wen, Q. Song, T. Zhang, B. P. Xie, X. G. Gong, and D. L. Feng, Nat. Commun. **5**, 5044 (2014).
[8] J. F. Ge, Z.-L. Liu, C. Liu, C.-L. Gao, D. Qian, Q.-K. Xue, Y. Liu, and J.-F. Jia, Nat. Mater. **14**, 285 (2015).
[9] J. J. Lee, F. T. Schmitt, R. G. Moore, S. Johnston, Y. T. Cui, W. Li, M. Yi, Z. K. Liu, M. Hashimoto, Y. Zhang, D. H. Lu, T. P. Devereaux, D.-H. Lee, and Z.-X. Shen, Nature (London) **515**, 245 (2014).
[10] H. Ding, Y.-F. Lv, K. Zhao, W.-L. Wang, L. Wang, C.-L. Song, X. Chen, X.-C. Ma, and Q.-K. Xue, Phys. Rev. Lett. **117**, 067001 (2016).
[11] S. Zhang, J. Guan, X. Jia, B. Liu, W. Wang, F. Li, L. Wang, X. Ma, Q. Xue, J. Zhang, E. W. Plummer, X. Zhu, and J. Guo, Phys. Rev. B **94**, 081116(R) (2016).
[12] Q. Song, T. L. Yu, X. Lou, B. P. Xie, H. C. Xu, C. H. P. Wen, Q. Yao, S. Y. Zhang, X. T. Zhu, J. D. Guo, R. Peng, and D. L. Feng, Nat. Commun. **10**, 758 (2019).
[13] F. Giustino, Rev. Mod. Phys. **89**, 015003 (2017).
[14] T. Valla, A. V. Fedorov, P. D. Johnson, S. Wells, B. O. Hulbert, L. Q. Li, G. D. Gu, and N. Koshizuka, Science **285**, 2110 (1999).
[15] A. Lanzara, P. V. Bogdanov, X. J. Zhou, S. A. Kellar, and Z.-X. Shen, Nature (London) **412**, 510 (2001).
[16] A. Damascelli, Z. Hussain, and Z.-X. Shen, Rev. Mod. Phys. **75**, 473 (2003).
[17] B. A. McDougall, T. Balasubramanian, and E. Jensen, Phys. Rev. B **51**, 13891(R) (1995).
[18] E. W. Plummer, J. Shi, S. J. Tang, E. Rotenberg, and S. D. Kevan, Prog. Surf. Sci. **74**, 251 (2003).
[19] E. Weschke, A. Y. Grigoriev, C. Schüßler-Langeheine, C. Mazumdar, R. Meier, S. Vandré, S. Ram, L. Kilian, G. Kaindl, and C. Sutter, Phys. Rev. Lett. **83**, 584 (1999).
[20] D. C. Koskenmaki and J. K. A. Gschneidner, in *Handbook on the Physics and Chemistry of Rare Earths* (Elsevier, New York, 1978), Vol. 1, Chap. 4, pp. 337–377.
[21] J. W. Allen and R. M. Martin, Phys. Rev. Lett. **49**, 1106 (1982).
[22] Y. Wu, F. Yuan, P. Li, Z.-G. Xiao, H. Zheng, Q. Yuan, C. Cao, Y.-F. Yang, and Y. Liu, Nat. Commun. **12**, 2520 (2021).
[23] J. Song, G. Fabbris, W. Bi, D. Haskel, and J. S. Schilling, Phys. Rev. Lett. **121**, 037004 (2018).
[24] D. Wegner, A. Bauer, and G. Kaindl, Phys. Rev. Lett. **94**, 126804 (2005).
[25] Y. S. Dedkov, D. Vyalikh, M. Weser, M. Holder, S. Molodtsov, C. Laubschat, Y. Kucherenko, and M. Fonin, Surf. Sci. **604**, 269 (2010).
[26] F. Offi, P. Vilmercati, L. Petaccia, S. Gorovikov, A. Ruocco, M. I. Trioni, A. Rizzo, A. Goldoni, G. Stefani, G. Panaccione, and S. Iacobucci, Phys. Rev. B **85**, 115108 (2012).
[27] See Supplemental Material at http://link.aps.org/supplemental/10.1103/PhysRevB.104.L161402 for more growth and measurement details.
[28] Z. Zhang, Q. Niu, and C.-K. Shih, Phys. Rev. Lett. **80**, 5381 (1998).
[29] L. Gavioli, K. R. Kimberlin, M. C. Tringides, J. F. Wendelken, and Z. Zhang, Phys. Rev. Lett. **82**, 129 (1999).
[30] Y. Liu, T. Miller, and T. C. Chiang, J. Phys.: Condens. Matter **23**, 365302 (2011).
[31] M. Hupalo, V. Yeh, L. Berbil-Bautista, S. Kremmer, E. Abram, and M. C. Tringides, Phys. Rev. B **64**, 155307 (2001).

[32] H. Hong, C.-M. Wei, M. Y. Chou, Z. Wu, L. Basile, H. Chen, M. Holt, and T.-C. Chiang, Phys. Rev. Lett. **90**, 076104 (2003).
[33] T.-C. Chiang, Surf. Sci. Rep. **39**, 181 (2000).
[34] M. Ogawa, A. Gray, P. M. Sheverdyaeva, P. Moras, H. Hong, L.-C. Huang, S.-J. Tang, K. Kobayashi, C. Carbone, T.-C. Chiang, and I. Matsuda, Phys. Rev. Lett. **109**, 026802 (2012).
[35] J. K. Kawasaki, C. H. Kim, J. N. Nelson, S. Crisp, C. J. Zollner, E. Biegenwald, J. T. Heron, C. J. Fennie, D. G. Schlom, and K. M. Shen, Phys. Rev. Lett. **121**, 176802 (2018).
[36] S. Gao, F. Flicker, R. Sankar, H. Zhao, Z. Ren, B. Rachmilowitz, S. Balachandar, F. Chou, K. S. Burch, Z. Wang, J. van Wezel, and I. Zeljkovic, Proc. Natl. Acad. Sci. USA **115**, 6986 (2018).
[37] X. J. Zhang and C. L. Chen, J. Low Temp. Phys. **169**, 40 (2012).
[38] M. Mohr, J. Maultzsch, E. Dobardžić, S. Reich, I. Milošević, M. Damnjanović, A. Bosak, M. Krisch, and C. Thomsen, Phys. Rev. B **76**, 035439 (2007).
[39] A. Grüneis, J. Serrano, A. Bosak, M. Lazzeri, S. L. Molodtsov, L. Wirtz, C. Attaccalite, M. Krisch, A. Rubio, F. Mauri, and T. Pichler, Phys. Rev. B **80**, 085423 (2009).
[40] D. H. Lee, Chin. Phys. B **24**, 117405 (2015).
[41] Z.-X. Li, T. P. Devereaux, and D.-H. Lee, Phys. Rev. B **100**, 241101(R) (2019).
[42] Y. Zhang, V. W. Brar, F. Wang, C. Girit, Y. Yayon, M. Panlasigui, A. Zettl, and M. F. Crommie, Nat. Phys. **4**, 627 (2008).
[43] V. W. Brar, S. Wickenburg, M. Panlasigui, C.-H. Park, T. O. Wehling, Y. Zhang, R. Decker, C. Girit, A. V. Balatsky, S. G. Louie, A. Zettl, and M. F. Crommie, Phys. Rev. Lett. **104**, 036805 (2010).
[44] C.-L. Song, Y.-L. Wang, Y.-P. Jiang, Z. Li, L. Wang, K. He, X. Chen, J. E. Hoffman, X.-C. Ma, and Q.-K. Xue, Phys. Rev. Lett. **112**, 057002 (2014).
[45] Y. Liu, L. Zhang, M. K. Brinkley, G. Bian, T. Miller, and T.-C. Chiang, Phys. Rev. Lett. **105**, 136804 (2010).
[46] S. Y. Zhou, D. A. Siegel, A. V. Fedorov, and A. Lanzara, Phys. Rev. B **78**, 193404 (2008).
[47] J. E. Ortega and F. J. Himpsel, Phys. Rev. Lett. **69**, 844 (1992).
[48] N. J. Speer, S.-J. Tang, T. Miller, and T.-C. Chiang, Science **314**, 804 (2006).
[49] H. Shishido, T. Shibauchi, K. Yasu, T. Kato, H. Kontani, T. Terashima, and Y. Matsuda, Science **327**, 980 (2010).